Atmospheric Research 334 (2026) 108782

Contents lists available at ScienceDirect

Atmospheric Research

journal homepage: www.elsevier.com/locate/atmosres

Impacts of full-scale turbulence intermittency on land-atmosphere interactions in the hinterland of the Taklimakan Desert

Peixuan Kang [a,b], Yan Ren [a,b,*], Hongsheng Zhang [c], Wei Wei [d], Yue Xu [a,b], Ali Mamtimin [e,f,g], Yu Wang [e,f,g], Meiqi Song [e,f,g], Jiening Liang [b], Lei Zhang [a,b], Jianping Huang [a]

[a] Collaborative Innovation Center for Western Ecological Safety, Lanzhou University, Lanzhou 730000, China
[b] Key Laboratory for Semi-Arid Climate Change of the Ministry of Education, College of Atmospheric Sciences, Lanzhou University, Lanzhou 730000, China
[c] Laboratory for Climate and Ocean-Atmosphere Studies, Department of Atmospheric and Oceanic Sciences, School of Physics, Peking University, Beijing 100081, China
[d] State Key Laboratory of Severe Weather and Key Laboratory of Atmospheric Chemistry of CMA, Chinese Academy of Meteorological Sciences, China Meteorological Administration (CMA), Beijing, China
[e] Institute of Desert Meteorology, China Meteorological Administration, Urumqi 830002, China
[f] National Observation and Research Station of Desert Meteorology, Taklimakan Desert of Xinjiang, Urumqi 830002, China
[g] Xinjiang Key Laboratory of Desert Meteorology and Sandstorm, Urumqi 830002, China

ARTICLE INFO

Keywords:
Land-atmosphere exchange
Turbulence intermittency
Sub-mesoscale motions
Turbulent energy spectrum
Taklimakan Desert

ABSTRACT

The Taklimakan Desert is characterized by strong thermal forcing and a heterogeneous underlying surface, where sub-mesoscale motions and turbulence intermittency occur frequently and interfere with the accurate evaluation of land-atmosphere exchange fluxes. Based on a summer observation campaign at Tazhong Station, this study develops a spectra-based automatic classification algorithm that classifies the influence of sub-mesoscale motions and turbulence intermittency into four regimes. Regime 1, no intermittency and no influence of sub-mesoscale motions; Regime 2, large-scale intermittency with influence of sub-mesoscale motions; Regime 3, small-scale intermittency without influence of sub-mesoscale motions; and Regime 4, full-scale intermittency with influence of sub-mesoscale motions. The classification results show that Regimes 2 and 4, corresponding to large-scale and full-scale intermittency, occur most frequently. Large-scale intermittency can occur under almost any wind speed and stability conditions, but is stronger under nocturnal weak-wind stable conditions. Full-scale intermittency occurs predominantly under nocturnal weak winds or under near-neutral conditions with relatively strong winds during the day-night transition. For Regimes 2 and 4, empirical relationships are derived that relate large-scale and small-scale intermittency strengths to wind speed and wind shear, enabling automatic identification of turbulent intermittency. By removing sub-mesoscale motions, turbulent statistics are corrected for each regime and empirical correction schemes are proposed, which effectively improve estimates of turbulence intensity and counter-gradient transport in Regimes 2 and 4. These results deepen understanding of turbulent intermittency over the Taklimakan Desert and improve parameterizations of turbulent transport, with important implications for weather and climate predictions.

1. Introduction

The Taklimakan Desert (TD), located in Central Asia, is the world's second-largest shifting sand desert, where dust events and seasonal local dust storms occur frequently (Gong et al., 2003; Zhang et al., 2003; Chen et al., 2017a, 2017b). Dust particles from the Taklimakan Desert can be lifted to high altitudes and subsequently transported over long distances, which not only affects the ecological environment and human health throughout East Asia, but also makes the desert an important source region of global dust aerosols (Zhang et al., 2008; Hu et al., 2019; Meng et al., 2020; Xiong et al., 2023; Elshora et al., 2024). This is closely related to the unique structure of the atmospheric boundary layer over the Taklimakan Desert. In this region, the boundary layer and turbulent motions are primarily characterized by strong thermal forcing and pronounced non-stationarity, with boundary layer heights typically reaching 4–6 km (Wang et al., 2016, 2019). The atmospheric boundary layer is more stable at night and more unstable during the daytime, exerting important influences on regional weather, climate, and

* Corresponding author at: Collaborative Innovation Center for Western Ecological Safety, Lanzhou University, Lanzhou 730000, China.
E-mail address: ry@lzu.edu.cn (Y. Ren).

https://doi.org/10.1016/j.atmosres.2026.108782
Received 8 December 2025; Received in revised form 4 January 2026; Accepted 15 January 2026
Available online 16 January 2026

atmospheric circulation. Therefore, investigating the characteristics and mechanisms of turbulent transport in the atmospheric boundary layer over the Taklimakan Desert is of great importance for improving regional weather forecasting, climate prediction, and air quality assessment, and even for understanding its environmental effects on the global scale.

As the dynamical core of land-atmosphere exchange, turbulence in the atmospheric boundary layer directly regulates the fluxes of momentum, heat, water vapor, and trace gases between the surface and the atmosphere, and it also determines aerosol fluxes, vertical distributions, and near-surface concentrations (Conte et al., 2021; Ren et al., 2021; Wei et al., 2022). Therefore, accurate estimation and physical characterization of turbulent statistical quantities are prerequisites for credible atmospheric boundary layer parameterizations and numerical models. However, in practical applications, surface heterogeneity and non-stationary atmospheric conditions increase the scatter in estimates of turbulent statistics and enhance the uncertainty of turbulence similarity functions (Vickers and Mahrt, 1997; Bou-Zeid et al., 2020; Pfister et al., 2021; Liu et al., 2025). If not properly identified and corrected, these biases propagate from the observational stage into parameterizations and numerical simulations, potentially affecting subsequent model applications. Previous studies have shown that substantial differences in sensible heat flux can cause marked differences in the daytime growth of the convective boundary layer over the Taklimakan Desert in summer (Xu et al., 2018). Uncorrected biases also interfere with the calibration of key land-surface parameters, such as surface roughness and soil thermal and moisture properties, in desert regions (Liu et al., 2012). Accurate estimation of turbulent quantities in the Taklimakan Desert is therefore essential for understanding land atmosphere interactions in desert areas and for improving parameterization schemes used in regional and global models.

In the atmospheric boundary layer over the Taklimakan Desert, which is characterized by strong thermal forcing and pronounced non-stationarity, biases in the evaluation of turbulent transport are strongly influenced by sub-mesoscale motions and turbulence intermittency. Mahrt (1989, 1999) divided turbulence intermittency into large-scale intermittency and small-scale intermittency. Large-scale intermittency refers to brief bursts of turbulence embedded within periods of relatively weak fluctuations (Mahrt, 1999; Van de Wiel et al., 2002; Ohya et al., 2008). It is often driven by non-stationarity imposed on the mean flow by motions with time scales longer than those of turbulence, i.e., sub-mesoscale motions such as gravity waves, density currents, and microfronts (Mahrt, 2010; Sun et al., 2015a, 2015b; Cava et al., 2019; Vercauteren et al., 2019; Mahrt and Bou-Zeid, 2020). Sub-mesoscale motions commonly manifest as an anomalous enhancement of low-frequency energy in the spectrum (Lan et al., 2018; Lehner and Rotach, 2023). Removing the contributions of sub-mesoscale motions from turbulent time series can effectively correct biases in the estimated turbulent statistics and thus yield more intrinsic turbulence statistics. Durden et al. (2013) found that the presence of sub-mesoscale motions can increase turbulent statistical quantities by about 50%. Ren et al. (2019) further reported that differences in the underlying surface affect the correction results: over a suburban surface, turbulent momentum, heat, and water vapor fluxes are overestimated by about 13%, 12%, and 15%, respectively.

By contrast, intermittency that occurs within large eddies is referred to as small-scale intermittency (Mahrt, 1999) and is an intrinsic component of fine-scale turbulence (Kolmogorov, 1962; Obukhov, 1962). Small-scale intermittency is often diagnosed from variations in physical quantities in the turbulent field: the energy dissipation rate deviates from a constant (Meneveau and Sreenivasan, 1991); statistical quantities exhibit non-Gaussian probability distributions (Sorriso-Valvo et al., 2000; Chevillard et al., 2006); and the scaling properties depart from the Kolmogorov similarity laws (Sreenivasan and Kailasnath, 1993; Klipp and Mahrt, 2004). Theoretically, the inertial subrange of the turbulent energy spectrum is commonly assumed to be isotropic (Kolmogorov, 1941). However, observations show that even within this range significant anisotropy and small-scale intermittency may still be present (Wei et al., 2019). This challenges assumptions commonly used in numerical modeling frameworks (Banhos and Matheou, 2025). At the same time, commonly used spectral correction procedures based on the Kaimal et al. (1972) spectral model for turbulence data preprocessing (Kroon et al., 2010) generally do not explicitly account for the high-frequency deviations induced by small-scale intermittency. As a result, the preprocessed data may fail to faithfully represent small-scale features, thereby reducing the credibility of subsequent analyses or simulations. Desert regions are characterized by strong thermal forcing and deep boundary layers, which can complicate the interactions between turbulence and sub-mesoscale motions. Improving our understanding of turbulence intermittency over the Taklimakan Desert is therefore important for further improving parameterization schemes in numerical models.

However, to date, studies on turbulence intermittency over the Taklimakan Desert have received relatively little attention. Most existing works have focused only on either large-scale intermittency or small-scale intermittency, and the differences between intermittency at different scales remain unclear. Against this background, the present study starts from the spectral characteristics of turbulence and quantitatively investigates the impact of sub-mesoscale motions and turbulence intermittency within a unified theoretical and methodological framework. Within this framework, we develop an automatic classification algorithm for turbulence intermittency regimes, which objectively identifies large-scale intermittency, small-scale intermittency, and full-scale intermittency, where large-scale and small-scale intermittency coexist.

Specifically, this study (1) quantifies the occurrence frequency of each regime and its associated wind speed, wind shear, and stability conditions; (2) establishes empirical relationships linking intermittency strength to wind speed and wind shear, thereby facilitating the diagnosis of intermittency from routinely available meteorological variables; and (3) proposes regime-dependent correction relationships for land-atmosphere exchange quantities, with implications for observational post-processing and potential model parameterizations. The remainder of this paper is organized as follows. Section 2 describes the field campaign and methods, Section 3 presents the results and discussion, and Section 4 summarizes the main conclusions.

2. Data and methods

2.1. Field campaign

From 1 to 31 July 2023, an intensive summer observation campaign of turbulence in the boundary layer was carried out at Tazhong meteorological station (39°00′N, 83°40′E). The observation period was broadly consistent with the long-term July climatology and is therefore considered representative of typical summer conditions. The Taklimakan Desert is located in the hinterland of the Tarim Basin and is surrounded by the Tianshan, Kunlun, and Pamir Mountains. The region has a typical warm-temperate arid desert climate, with a mean annual precipitation of only 25.9 mm and a potential evaporation as high as 3812.3 mm, indicating an extremely dry environment. Surface vegetation is sparse, and the surrounding area is covered by undulating shifting sand dunes. Tazhong Station (Fig. 1a), located more than 200 km from the desert margin in the hinterland of the Taklimakan Desert, is currently the only long-term field scientific observation station in the world built deep within active sand and is therefore highly representative.

The observational system consists of a 10 m meteorological tower and an independent eddy-covariance system (Fig. 1b). The meteorological tower has five observation levels at heights of 0.5, 1, 2, 4, and 10 m. At each level, temperature and humidity sensors (HMP45C, Vaisala *Co*., Finland) and wind speed and direction sensors (Wind Observer II-

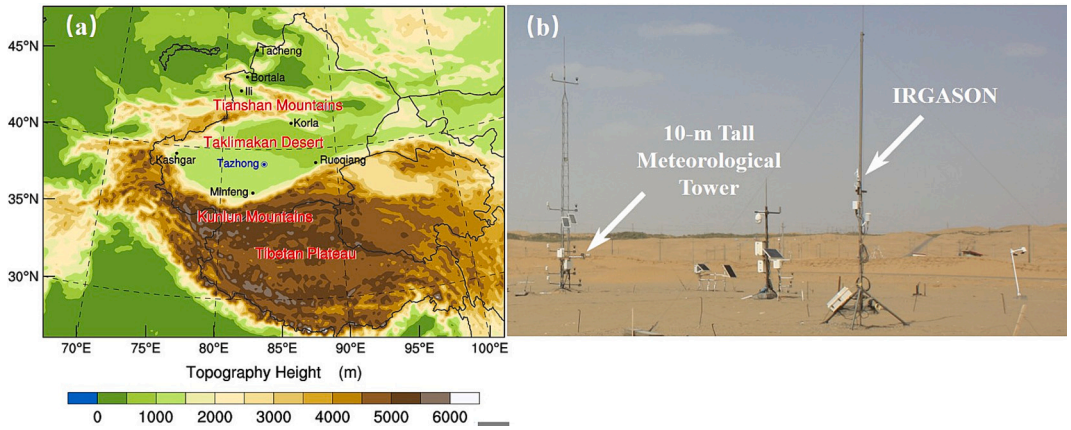

Fig. 1. (a) Topographic map around the Taklimakan Desert and the location of the Tazhong meteorological station (from Wang et al., 2019); (b)10 m meteorological tower and eddy-covariance system.

65, Gill Instruments Ltd., UK) were installed to observe the vertical variations of near-surface air temperature, humidity, wind speed, and wind direction. The gradients of temperature and wind speed were calculated from the measurements at 2 m and 10 m. The eddy-covariance system was mounted on an independent frame at a height of about 3 m above the ground and consists of a three-dimensional sonic anemometer and an open-path gas analyzer (IRGASON, Campbell Scientific Inc., USA). It sampled at 10 Hz and was used to obtain high-frequency turbulent data, including the three components of wind velocity, temperature, and water vapor and carbon dioxide concentrations.

2.2. Quantitative characterization of the strength of turbulence intermittency

The 10 Hz raw turbulence data were pre-processed using the EddyPro software (v 6.2.1, LI-COR Bioscience Inc., USA). The averaging interval was set to 30 min, and the main processing steps included error flags, despiking, double coordinate rotation, and detrending.

In this study, two indices are used: the Local Intermittency Strength of Turbulence (LIST; Ren et al., 2019) to characterize the strength of large-scale intermittency, and the Intermittency Factor (IF; Wei et al., 2019) to quantify the strength of small-scale intermittency.

1) Local Intermittency Strength of Turbulence(LIST)

In this study, the LIST index is calculated using an automatic algorithm for the separation and reconstruction of sub-mesoscale and turbulent motions (SMT; Ren et al., 2019, 2023). This algorithm is based on the Hilbert-Huang transform and examines the second-order Hilbert spectrum of 30 min time series of meteorological fluctuations (u', v', w', potential temperature θ', water vapor density q', and $CO_2{}'$). Frequency intervals in the second-order Hilbert spectrum where the slope is close to zero or the values remain nearly constant are identified as spectral gaps. The corresponding gap frequency is multiplied by the low-frequency growth portion of the energy spectrum, and this gap frequency is then taken as the critical frequency separating sub-mesoscale motions from turbulent motions. The components with frequencies lower than the critical frequency are defined as sub-mesoscale motion signals $u_{sub}{}'$, $v_{sub}{}'$, $w_{sub}{}'$, $\theta_{sub}{}'$, $q_{sub}{}'$, and $CO_{2sub}{}'$, whereas those with frequencies higher than the critical frequency are defined as turbulent motion signals $u_{turb}{}'$, $v_{turb}{}'$, $w_{turb}{}'$, $\theta_{turb}{}'$, and $CO_{2turb}{}'$. The SMT algorithm yields pure turbulent motions with sub-mesoscale motions removed. The kinetic energy of turbulent motions (TKE) and the kinetic energy of sub-mesoscale motions (SKE) are then defined based on the separated turbulent and sub-mesoscale components:

$$TKE = \frac{1}{2}\left(\overline{u_{turb}^{'2}} + \overline{v_{turb}^{'2}} + \overline{w_{turb}^{'2}}\right) \tag{1}$$

$$SKE = \frac{1}{2}\left(\overline{u_{sub}^{'2}} + \overline{v_{sub}^{'2}} + \overline{w_{sub}^{'2}}\right) \tag{2}$$

Furthermore, LIST is given by:

$$LIST = \frac{\sqrt{TKE}}{\sqrt{TKE + SKE}} \tag{3}$$

Physically, it is the ratio of the intensity of turbulent motions to that of sub-mesoscale motions in the fluctuation signals of meteorological variables, and thus characterizes the strength of turbulent motions in the original fluctuation signal. Values of LIST approaching 1 indicate that turbulent motions dominate the original fluctuations and the influence of sub-mesoscale motions is weak. In contrast, smaller LIST values indicate a reduced contribution from turbulent motions and a stronger influence of sub-mesoscale motions.

2) Intermittency Factor(IF)

IF (Wei et al., 2019) quantifies intermittency by measuring the deviation of the scaling exponent in the Hilbert spectrum from the Kolmogorov (1941, K41) linear scaling. Extending the application of IF to different turbulent variables, we define IF_x (as)

$$IF_x = (\xi(q) - 1) - \frac{q}{3} \tag{4}$$

where x denotes u', v', w', θ', q', and $CO_2{}'$. The function $\xi(q)$ is the scaling exponent obtained from the Hilbert spectral analysis of order q, and it describes the distribution of turbulent energy across different scales (frequencies). $\frac{q}{3}$ is the scaling exponent predicted by the K41 theory for homogeneous and isotropic turbulence. In this study, we set $q = 2$, i.e., we consider only the second-order Hilbert spectrum, in order to keep the analysis consistent with the framework used for spectral gap identification. Smaller values of IF_x indicate a larger deviation from K41, meaning that the inertial subrange part of the energy spectrum does not follow the scaling law $E(k) \propto k^{-5/3}$, and the small-scale intermittency is stronger.

In analogy with the definition of LIST, the composite IF is defined as follows:

$$IF = \frac{1}{3}\left(IF_{u'} + IF_{v'} + IF_{w'}\right) \tag{5}$$

2.3. An automated method for classifying turbulent intermittency regimes

Spectral analysis of the experimental data shows that intermittency can be classified into four regimes: no intermittency (Regime 1), large-scale intermittency (Regime 2), small-scale intermittency (Regime 3), and full-scale intermittency (Regime 4), in which large-scale and small-scale intermittency coexist. In the energy spectrum, large-scale intermittency acts mainly in the energy-containing range and manifests as a deviation from the classical spectrum proposed by Kaimal et al. (1972) at low frequencies, with an abnormal increase in energy toward lower frequencies. Small-scale intermittency primarily affects the inertial subrange, where the K41 scaling is not satisfied and the spectral slope deviates significantly from the theoretical value of −5/3.

To enable rapid diagnosis of turbulence states based on spectral characteristics, identify the dominant intermittency scales, and locate the key physical processes associated with Regimes 2–4, we develop an automatic classification algorithm for turbulence intermittency. A flowchart of this procedure is shown in Fig. 2. Specifically, (a) the high-frequency fluctuation data preprocessed by EddyPro are first input, and the index IF_x is calculated according to Section 2.2. The probability distributions of IF_x for all data of each variable are compiled (figure not shown). Because the range and shape of the IF_x distributions differ among velocity components and scalars, using a single universal percentile would not yield an equivalent criterion for identifying strong departures across variables. The thresholds are therefore chosen by considering the robustness of inertial-subrange slope fitting for each variable, which is generally more stable for horizontal velocity components than for the vertical velocity component and scalars. Based on the characteristics of each variable, the IF_x values corresponding to the lowest 15% (for u and v), 30% (for w), or 40% (for θ, q, and CO_2) of the distribution are taken as the threshold x_{th} for that variable. This threshold is used to judge whether the spectral slope in the inertial subrange deviates significantly from −5/3. (b) IF_x is then compared with the threshold x_{th}. If the IF_xvalue of the input data is smaller than the

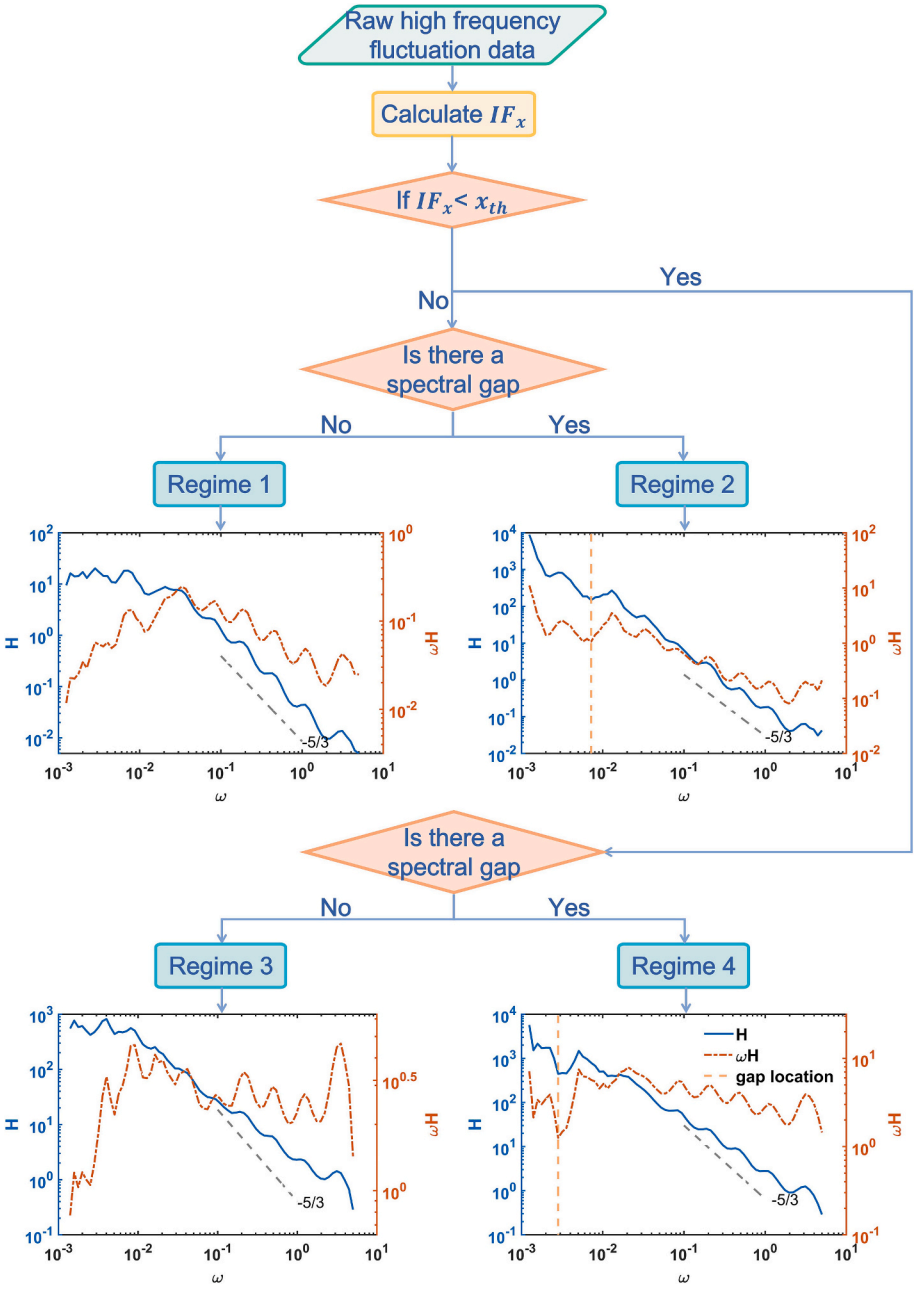

Fig. 2. Flowchart of the automatic classification algorithm for regimes of turbulence intermittency.

threshold, small-scale intermittency is considered to be present. (c) The SMT algorithm is then used to determine whether a spectral gap exists. If a spectral gap is identified, large-scale intermittency is considered to be present.

When the spectral slope in the inertial subrange is approximately −5/3 and no spectral gap exists, the case is classified as Regime 1, corresponding to conditions without intermittency. When IF_x is smaller than the threshold and a spectral gap is present, the case is regarded as having only large-scale intermittency and is assigned to Regime 2. When IF_x is larger than the threshold and no spectral gap is present, the case is regarded as having only small-scale intermittency and is assigned to Regime 3. When the spectral slope in the inertial subrange deviates markedly from −5/3 and a spectral gap is present, the case is classified as Regime 4, corresponding to full-scale intermittency in which both large-scale and small-scale intermittency coexist. To ensure the reliability of the classification, all results were manually checked, and the subsequent analysis is based on the revised classification. The occurrence frequencies of the four regimes differ slightly among variables. For Regime 1, the fractions for u, v, w, θ, q, and CO_2 are 8.5%, 5.2%, 12.7%, 9.7%, 2.5%, and 4.0%, respectively; for Regime 2, they are 78.9%, 79.2%, 56.1%, 52.1%, 50.2%, and 44.7%; for Regime 3, 1.4%, 2.0%, 10.0%, 6.7%, 2.9%, and 3.5%; and for Regime 4, 11.2%, 13.7%, 21.1%, 31.4%, 44.3%, and 47.8%, respectively. Except for CO_2, for which the fraction of Regime 4 is slightly larger than that of Regime 2, Regime 2 has the largest fraction for all variables, with the highest fractions for the horizontal wind components. These results indicate that large-scale intermittency occurs most frequently, that full-scale intermittency is much more prevalent for scalars than for wind speed, and that cases with only small-scale intermittency or without intermittency are generally rare. Therefore, Regime 2 and Regime 4 are the primary targets for correction in this study.

To further investigate the characteristics of fluctuations under different regimes, Fig. 3 shows time series of the original horizontal wind speed fluctuations u' and temperature fluctuations θ'. For Regime 1, both u' and θ' are very steady, with no pronounced trend. Compared with Regime 1, Regime 2 shows a pronounced low-frequency trend superimposed on the fluctuations and is influenced by "dirty waves" whose amplitude and period vary in time. The low-frequency control is more evident in θ'. Regime 3 shows no obvious upward or downward trend, but is characterized by intermittent strong pulses, large variance, and asymmetric amplitudes, indicating that it is dominated by small-scale intermittency. In addition, the fluctuation range of u' is clearly larger than that of θ'. Regime 4 displays the largest amplitude variations, with evident aperiodic behavior and strong coupling across scales, so that slowly varying low-frequency components coexist with intermittent bursts. Across the four regimes, the fluctuation characteristics of

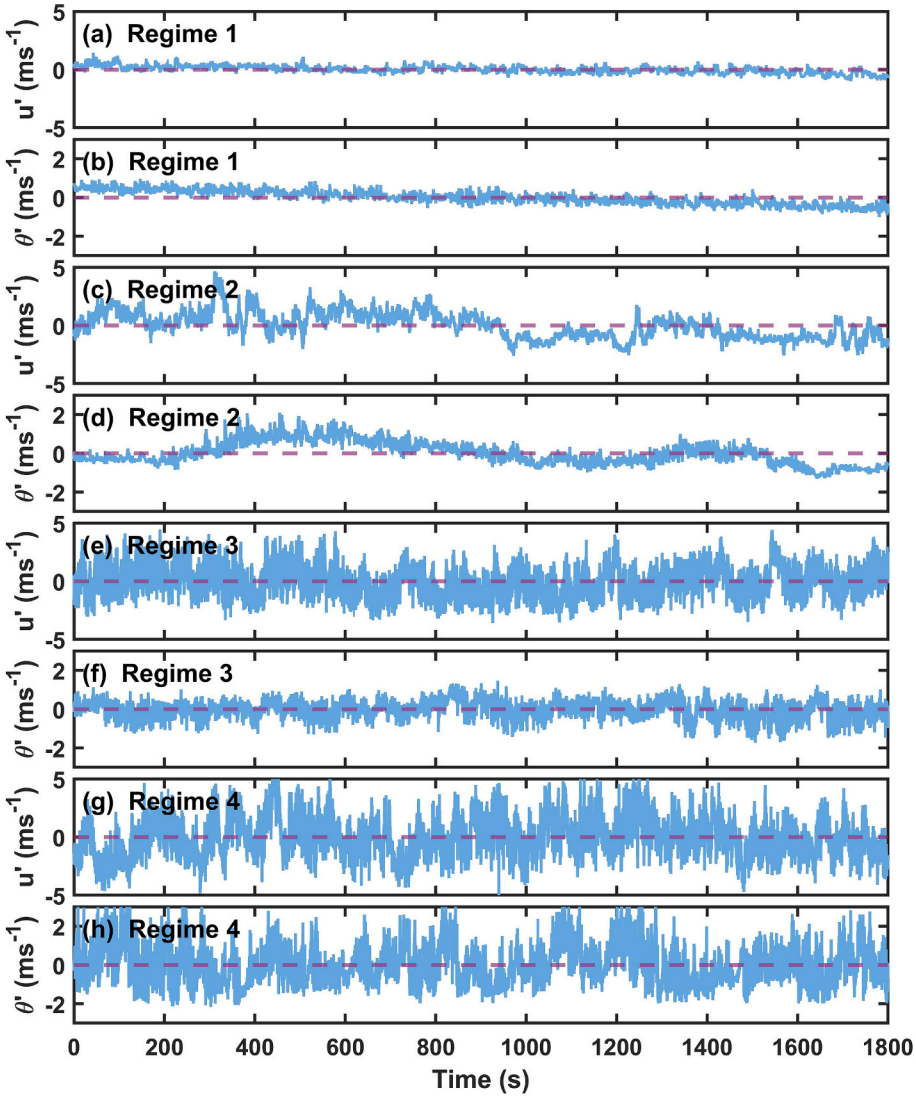

Fig. 3. Time series of horizontal wind speed fluctuations u′ (a, c, e, g) and temperature fluctuations θ′ (b, d, f, h) for the different regimes.

momentum and scalar variables differ markedly and are consistent with theoretical expectations, indicating that the classification scheme is reliable.

3. Results

3.1. Meteorological conditions across regimes and their relationship with intermittency strength

To begin with, characteristics of the atmospheric boundary layer for the four regimes during the campaign are analyzed. These characteristics provide a basis for interpreting the features of summer turbulence intermittency over the Taklimakan Desert. Fig. 4 shows the distributions of wind speed, friction velocity u_*, stability parameter ($\zeta = z/L$, where L is the Monin-Obukhov length defined as $L = -\frac{u_*^3}{\kappa \frac{g}{\theta}\overline{w'\theta'}}$, $\kappa = 0.4$, and $z = 3\ m$ is the measurement height) and the intermittency indices LIST and IF for the four regimes. For u_* and z/L (Fig. 4b and c), results based on the original data and on the pure turbulent signals reconstructed using the SMT algorithm are plotted in brown and black, respectively. It is evident that, after removing sub-mesoscale motions, u_* decreases markedly, $|z/L|$ increases, and strongly stable or strongly unstable stratification occurs more frequently. The time series further indicate that the four regimes are dominated by Regime 2 (large-scale intermittency) and Regime 4 (full-scale intermittency). The meteorological conditions for each regime also differ. Regime 2 can occur under almost any wind speed and stability conditions, but under weak winds and a stably stratified nocturnal boundary layer, turbulent motions are suppressed by sub-mesoscale motions, leading to stronger large-scale intermittency, as reflected by smaller LIST values. Regime 4 occurs in two types of situations. The first situation corresponds to nighttime with weak winds, mainly reflecting apparent deviations of the spectral structure caused by non-stationarity and sub-mesoscale motions, with both LIST and IF taking relatively small values. The second corresponds to nearly neutral conditions with relatively high wind speed during the transition between day and night, where LIST is relatively large and IF is small, indicating enhanced genuine small-scale intermittency associated with localized dissipation.

Next, relationships between the intermittency strength indices (LIST and IF) for the four regimes and the mean meteorological fields of wind speed, wind shear, temperature gradient, and bulk Richardson number are examined, as shown in Fig. 5. It can be seen that intermittency strength also varies systematically with the mean meteorological conditions. For LIST, Regimes 2 and 4 exhibit almost identical trends, with LIST increasing as wind speed and wind shear increase. In Regime 2, LIST decreases with increasing temperature gradient, and Regime 4 shows essentially the same behavior. This indicates that large-scale intermittency, as well as the coexistence of large-scale and small-scale intermittency, occurs more readily under more stable conditions and lower wind speed. For IF, values in Regimes 1 and 2 are larger than those in Regimes 3 and 4. This is because, in the automatic classification algorithm, cases in Regimes 1 and 2 satisfy $IF_x > x_{th}$, implying that small-scale intermittency can be neglected to some extent. In Regime 2, IF decreases with increasing wind speed. In Regime 4, IF also decreases with increasing wind speed for both wind speeds greater than 3.5 m s^{-1} and those less than 3.5 m s^{-1}, corresponding to the two types of situations in which Regime 4 occurs. In Regime 2, IF decreases as wind shear increases, whereas in Regime 4 the decrease with wind shear is noticeably weaker. In Regime 2, IF decreases as $|Ri_b|$ decreases and reaches its minimum under nearly neutral conditions. Regime 4 mainly occurs under nearly neutral conditions, and IF tends to decrease with increasing bulk Richardson number.

Analyses of Figs. 4 and 5 further highlight the differences between large-scale and small-scale intermittency. Under stably stratified nocturnal conditions with weak winds, the influence of sub-mesoscale motions is stronger and large-scale intermittency is pronounced. The spectral structure is contaminated by sub-mesoscale motions, and the spectral slope in the inertial subrange deviates from the Kaimal spectrum. In such cases, IF takes smaller (more negative) values, which indicate enhanced small-scale intermittency. During the transition between day and night, nearly neutral conditions with relatively high wind speed are associated with turbulence that is more continuous at large

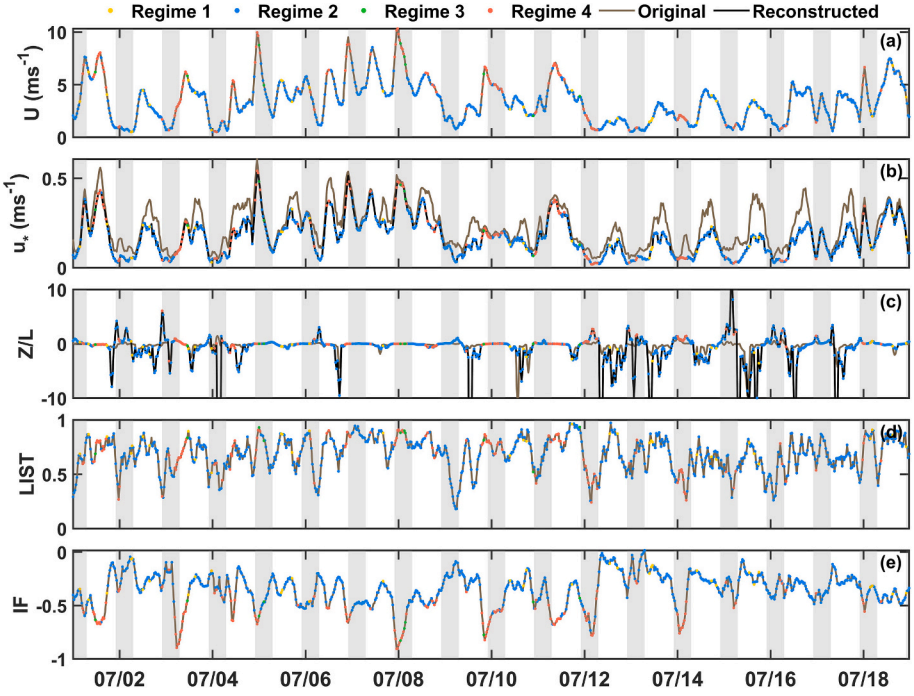

Fig. 4. Distributions of wind speed (a), friction velocity u_* (b), stability parameter ($\zeta = z/L$, $z = 3\ m$) (c) and intermittency indices LIST (d) and IF (e) for the four regimes. Yellow, blue, green, and red dots represent Regime 1, Regime 2, Regime 3, and Regime 4, respectively. The gray shading denotes night-time periods. (For interpretation of the references to colour in this figure legend, the reader is referred to the web version of this article.)

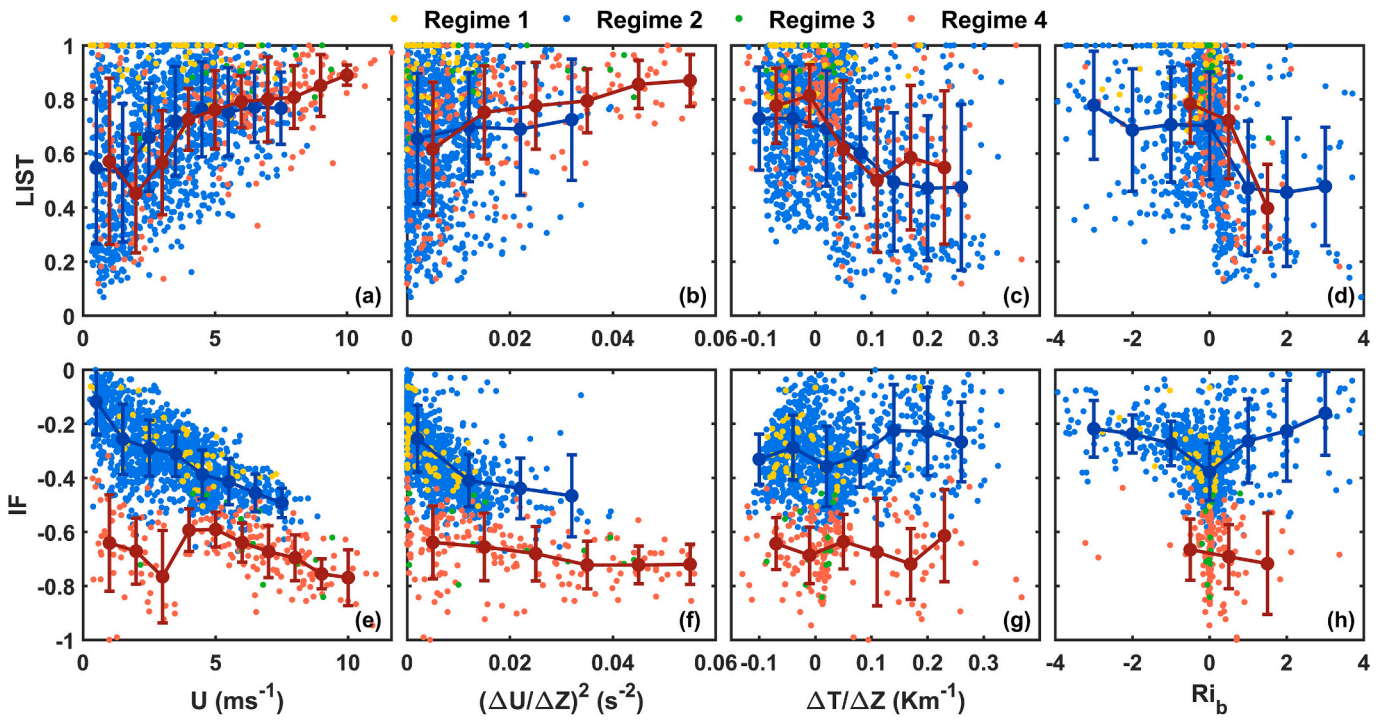

Fig. 5. Relationships of intermittency indices LIST and IF with mean wind speed (a, e), wind shear (b, f), temperature gradient (c, g), and bulk Richardson number (d, h). Yellow, blue, green, and red dots represent Regime 1, Regime 2, Regime 3, and Regime 4, respectively. Blue and red lines indicate the mean and standard deviation for Regime 2 and Regime 4. (For interpretation of the references to colour in this figure legend, the reader is referred to the web version of this article.)

scales (weaker large-scale intermittency), whereas energy dissipation is more uneven at fine scales. Small-scale anisotropy and strong dissipation lead to a departure of the spectral slope in the inertial subrange from the Kaimal reference slope, with IF decreasing and LIST increasing. In addition, based on the dependence of LIST and IF on wind speed and wind shear, the relationships are fitted with a power law of the form $y = ax^b$, and empirical relationships are obtained for Regimes 2 and 4. The corresponding coefficients are listed in Table 1.

3.2. Correction of turbulent statistical parameters for different regimes

This study further evaluates the influence of sub-mesoscale motions on turbulence statistics for the different regimes and proposes corresponding correction schemes. Fig. 6 shows the relationships between the original and corrected standard deviations of the fluctuations σ_u, σ_v, σ_w, σ_θ, σ_q, and σ_{CO_2} for Regimes 2 and 4. The horizontal axis denotes the standard deviation estimated from the original data, and the vertical axis denotes the standard deviation estimated from the reconstructed data. For Regime 2, the fitted slopes for σ_u, σ_v, σ_w, σ_θ, σ_q, and σ_{CO_2} are 0.6, 0.57, 0.98, 0.64, 0.33, and 0.53, respectively. Correspondingly, for Regime 4, the fitted slopes of the above meteorological variables are 0.73, 0.72, 0.99, 0.86, 0.1, and 0.81, respectively. For both Regimes 2 and 4, almost no overestimation is found for σ_w, indicating that intermittency induced by sub-mesoscale motions has little effect on the vertical velocity. All other variables exhibit substantial overestimation, with the largest effect on σ_q which indicates that turbulence intermittency has the strongest impact on water vapor in the desert region. The overestimation of σ_q in Regime 4 is larger than that in Regime 2, by about 90% and 67%, respectively. For all variables except σ_q, that is, σ_u, σ_v, σ_w, σ_θ, and σ_{CO_2}, the overestimation in Regime 2 is larger than that in Regime 4 and exceeds 10% for each of these variables. This indicates that under large-scale intermittency the influence of sub-mesoscale motions on these statistical quantities is stronger than under full-scale intermittency.

For the different regimes, the momentum fluxes $-\overline{u'w'}$ and $\overline{v'w'}$, the sensible heat flux $\overline{w'\theta'}$, the latent heat flux $\overline{w'q'}$, the CO_2 flux $\overline{w'co_2'}$ and turbulent kinetic energy TKE are also influenced differently by sub-mesoscale motions and turbulence intermittency. The relationships between the original and corrected values for these quantities are shown in

Table 1
Empirical relationships relating large-scale and small-scale intermittency strengths (LIST and IF) to wind speed and wind shear for Regimes 2 and 4, together with correction schemes for different turbulence statistics.

		Regime 2			Regime 4		
		$a, b/\beta_2$		R^2	$a, b/\beta_4$		R^2
LIST	U	0.57	0.16	0.86	0.47	0.27	0.83
	$(\Delta U/\Delta Z)^2$	0.80	0.03	0.84	1.29	0.14	0.97
IF	U (U > 3.5 m s^{-1})	−0.19	0.48	0.98	−0.36	0.32	0.94
	U (U < 3.5 m s^{-1})				−0.63	0.16	0.84
	$(\Delta U/\Delta Z)^2$	−0.98	0.21	0.97	−0.86	0.06	0.88
σ_u		0.60		0.57	0.73		0.69
σ_v		0.57		0.59	0.72		0.79
σ_w		0.98		1.00	0.99		1.00
σ_θ		0.64		0.70	0.86		0.96
σ_q		0.33		0.43	0.10		0.94
σ_{co_2}		0.53		0.80	0.81		0.94
$-\overline{u'w'}$		0.41		0.50	0.75		0.82
$\overline{v'w'}$		0.18		0.33	0.36		0.59
$\overline{w'\theta'}$		0.79		0.97	0.87		0.98
$\overline{w'q'}$		0.59		0.76	0.41		−0.66
$\overline{w'co_2'}$		0.66		0.20	0.79		0.82
TKE		0.43		0.62	0.59		0.70

Note. The fitted relationships relating large-scale and small-scale intermittency strengths (LIST and IF) to wind speed and wind shear are expressed as $y = ax^b$; the correction schemes for different turbulence statistics use $y = \beta x$. R^2 denotes the coefficient of determination.

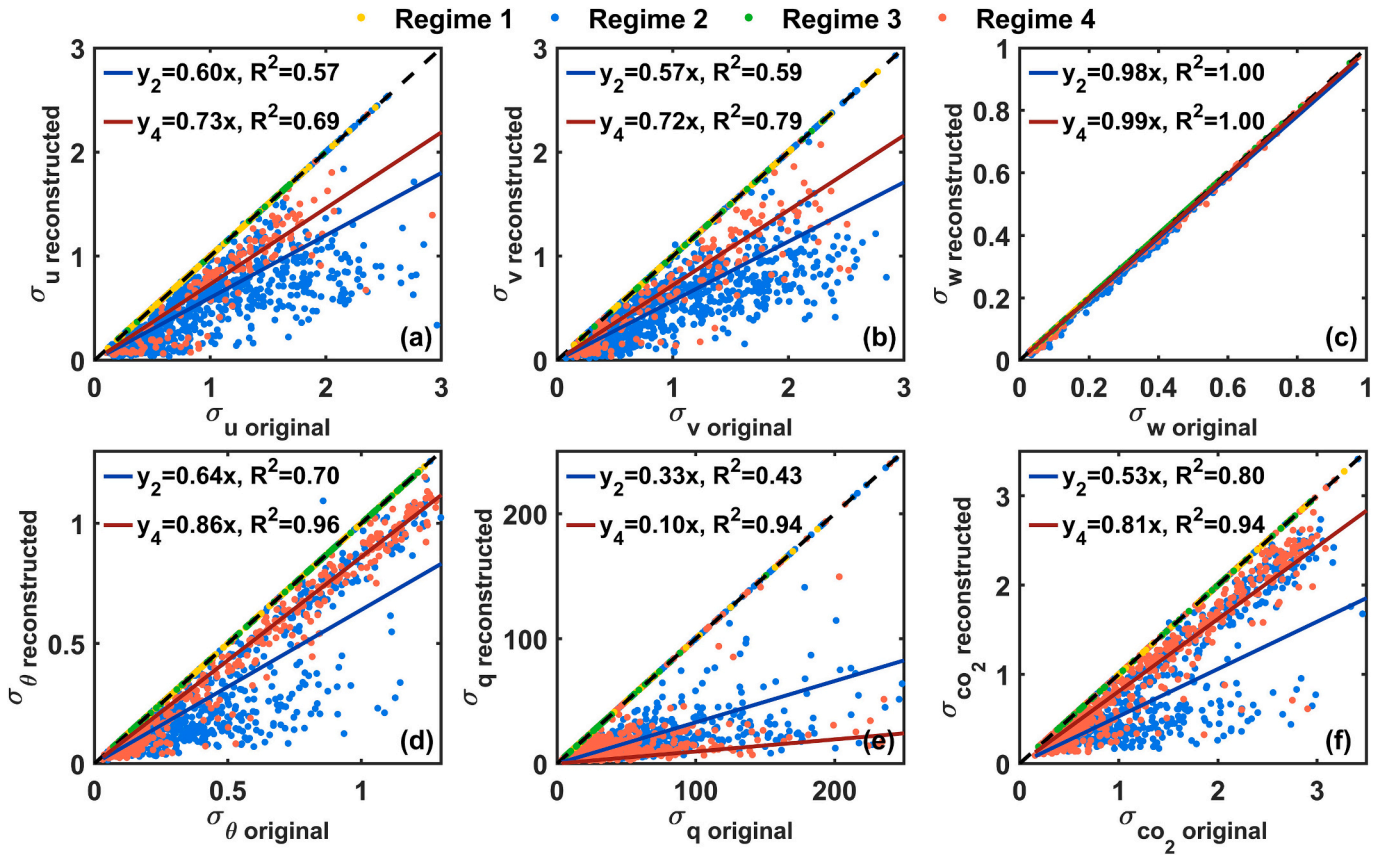

Fig. 6. Comparison between original and reconstructed standard deviations for the different regimes. Yellow, blue, green, and red dots represent Regime 1, Regime 2, Regime 3, and Regime 4, respectively. Blue and red lines show the linear fits for Regime 2 and Regime 4. (For interpretation of the references to colour in this figure legend, the reader is referred to the web version of this article.)

Fig. 7. For both Regimes 2 and 4, the slopes of the fitted lines are less than 1, indicating that the original data overestimate the turbulent fluxes and that the reconstructed data partly remove the influence of intermittency induced by sub-mesoscale motions. Except for the latent heat flux, for which the slope in Regime 4 is larger than that in Regime 2, the slopes for all other quantities are larger in Regime 2 than in Regime 4, which is consistent with the behavior of the standard deviations in Fig. 6. For Regime 2, the overestimation percentages are 59% for $\overline{-u'w'}$, 82% for $\overline{v'w'}$, 21% for $\overline{w'\theta'}$, 41% for $\overline{w'q'}$, 34% for $\overline{w'co_2'}$, and 57% for *TKE*. For Regime 4, the corresponding overestimations are 25%, 64%, 13%, 59%, 21%, and 41%. In the hinterland of the Taklimakan Desert, the impact of turbulence intermittency on momentum and water vapor transport is therefore much stronger than its impact on heat transport. Comparison between the original and corrected values of the different turbulence statistics shows that, because of the influence of sub-mesoscale motions on the fluctuations of each variable, the turbulent statistics obtained by the traditional eddy covariance method (the original values) are generally biased when large-scale or full-scale intermittency is present, and the magnitude of the bias differs among variables. It is thus necessary in practical applications to correct the fluxes according to the type of turbulence intermittency, and the specific correction schemes are summarized in Table 1.

3.3. *Performance and improvement of statistical parameters for different regimes*

Because of the presence of sub-mesoscale motions, the previous section applied corrections to fluxes and variances for the different regimes, and the changes in fluxes and variances in turn affect the related statistical quantities. To further understand the characteristics of different regimes of turbulence intermittency, boxplots are used to analyze the relationship between turbulence intensity (denoted as $V_{TKE} = \sqrt{TKE}$) and mean wind speed (U) for all data, Regime 2, and Regime 4. The height of the box, which represents the interquartile range (IQR), is determined by the spread of V_{TKE} within each bin of U. For a given U, larger variability in V_{TKE} leads to a taller box, and a greater overall spread is reflected in longer whiskers. After removing sub-mesoscale motions, V_{TKE} is effectively reduced under both unstable and stable conditions, and the degree of scatter is also reduced (see Fig. 8a and b). It is clear that, within the same wind speed range, V_{TKE} under unstable conditions is significantly larger than under stable conditions, and the data are more dispersed. The V_{TKE}-U relationship for Regime 2 is similar to that for all data, whereas Regime 4 under unstable conditions occurs only at relatively high wind speeds and is associated with stronger turbulence intensity. Under stable conditions, after removing sub-mesoscale motions, the increasing trend of V_{TKE} becomes more evident for both Regime 2 and Regime 4, and the transition point becomes clearer. When U is smaller than a wind speed threshold, V_{TKE} increases slowly. When U exceeds this threshold, V_{TKE} increases approximately linearly with wind speed. In addition, the threshold wind speeds differ between Regimes 2 and 4. The threshold for Regime 2 is smaller than that for Regime 4, at 2.4 m s^{-1} and 3.2 m s^{-1}, respectively.

To evaluate the effectiveness of the flux corrections, the fractions of counter-gradient momentum and sensible heat transport are calculated. According to turbulent gradient transport theory, the flux of a quantity induced by turbulence is proportional to the local mean gradient of that quantity, and the direction of transport is the same as the direction in which the quantity decreases, i.e., downgradient transport. A smaller fraction of counter-gradient transport indicates that the turbulent flux is less affected by sub-mesoscale motions and that the flux correction is

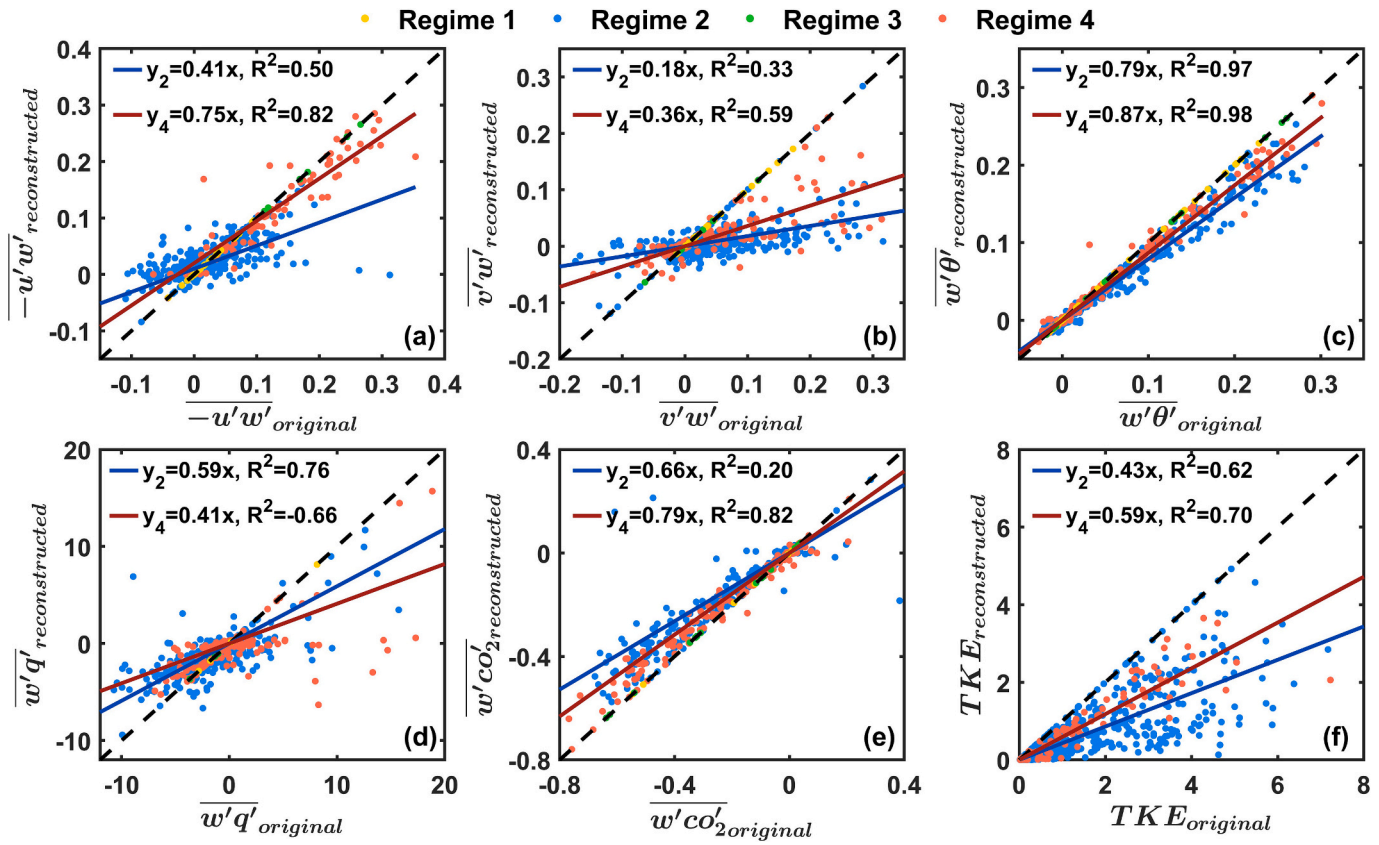

Fig. 7. Comparison between original and reconstructed turbulent fluxes and turbulent kinetic energy for the different regimes. Yellow, blue, green, and red dots represent Regime 1, Regime 2, Regime 3, and Regime 4, respectively. Blue and red lines show the linear fits for Regime 2 and Regime 4. (For interpretation of the references to colour in this figure legend, the reader is referred to the web version of this article.)

more effective. Fig. 9 shows the fractions of counter-gradient momentum flux and sensible heat flux as functions of the bulk Richardson number over the Taklimakan Desert in July 2023. After removing the sub-mesoscale component, the occurrence frequencies of counter-gradient momentum and sensible heat transport for Regimes 2 and 4 are clearly reduced. For the momentum flux (Fig. 9a and b), Regime 2 exhibits a relatively low fraction of counter-gradient transport under nearly neutral conditions. as stability or instability increases, the fraction of counter-gradient transport gradually increases. Regime 4 under stable conditions shows a similar behavior, but under unstable conditions the variation with stability is not obvious, and in this case the fraction of counter-gradient transport in Regime 2 is mostly larger than that in Regime 4. For the sensible heat flux, under unstable conditions the fractions of counter-gradient transport in Regimes 2 and 4 are essentially zero. Under strongly stable conditions, the fraction decreases markedly after removing sub-mesoscale motions. Under nearly neutral and weakly stable conditions, the fraction remains relatively high, likely because the sensible heat flux itself is small in magnitude in these regimes. In such cases, even relatively weak counter-gradient events account for a large proportion of the samples.

4. Conclusions

This study analyzes turbulence intermittency over the Taklimakan Desert based on observation campaign at Tazhong during 1–31 July 2023, and evaluates its impacts on turbulence statistics and related corrections.

On the basis of the observed fact that turbulent energy spectra deviate from the theoretical Kaimal spectrum under the influence of intermittency, an automatic classification algorithm for regimes of turbulence intermittency is proposed. The fluctuation characteristics of momentum and scalar variables differ markedly among the four regimes and are consistent with theoretical expectations, which supports the reliability of the classification scheme. Under nocturnal conditions with weak winds and stable stratification, large-scale intermittency is stronger, whereas full-scale intermittency occurs mainly under weak-wind nighttime conditions and under nearly neutral conditions with relatively high wind speed during the transition between day and night. In addition, empirical relationships are derived for Regimes 2 and 4 that relate the large-scale intermittency strength and small-scale intermittency strength to wind speed and wind shear.

After removing intermittency associated with sub-mesoscale motions, comparisons between the reconstructed and original data indicate that standard deviations, turbulent fluxes, and turbulent kinetic energy are generally overestimated in Regimes 2 and 4 when the original data are used. The impacts are strongest for momentum transport and water vapor transport, whereas heat transport is less affected. For most quantities, the biases are larger in Regime 2 than in Regime 4, suggesting a stronger influence of sub-mesoscale motions under large-scale intermittency. The effectiveness and physical consistency of the corrections are supported by two diagnostics. After correction, the relationship between turbulence intensity and wind speed shows markedly reduced scatter under both stable and unstable conditions. In addition, the fractions of counter-gradient momentum flux and counter-gradient sensible heat flux generally decrease in Regimes 2 and 4, indicating improved physical consistency of the corrected flux estimates.

To facilitate potential applications, we provide a conceptual schematic (Fig. 10) that summarizes the four regimes and illustrates an example workflow for diagnosing the most likely regime from routinely available variables and selecting the corresponding regime-dependent correction factor. This correction can then be incorporated into surface layer schemes by using corrected turbulent statistical parameters. It

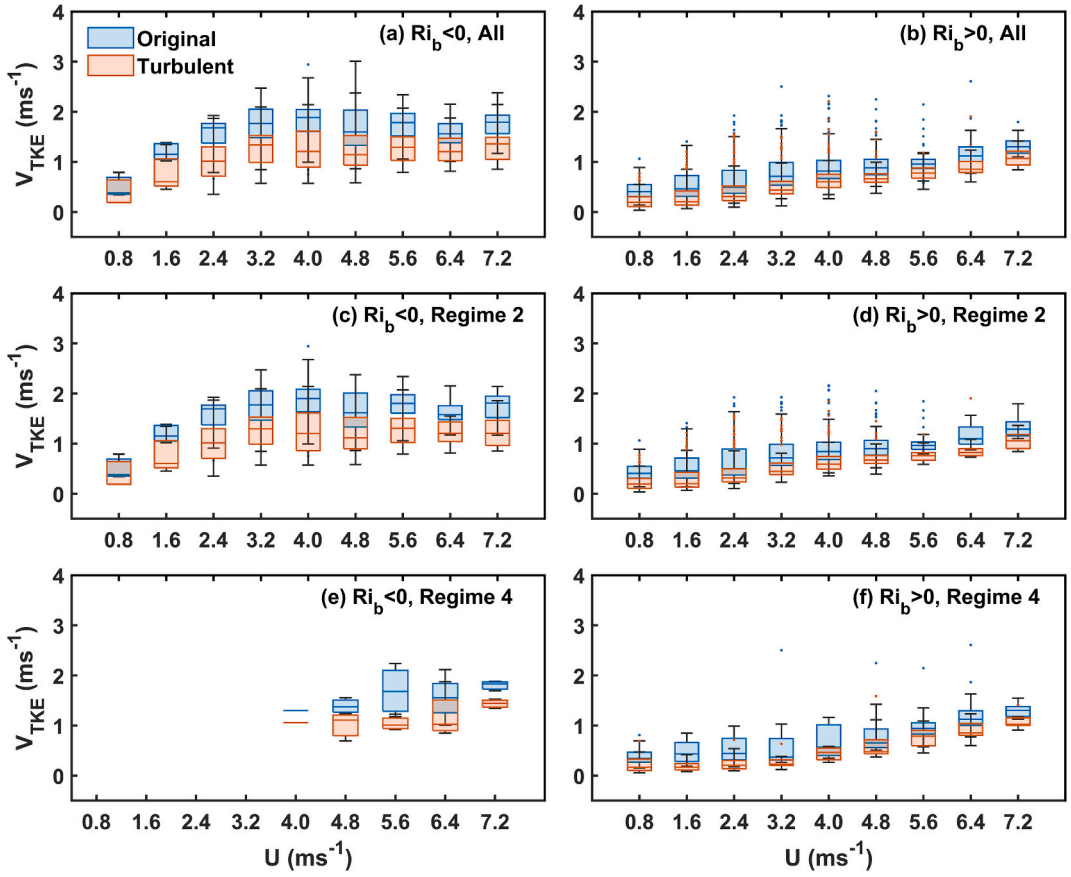

Fig. 8. Relationships between turbulence intensity (V_{TKE}) and mean wind speed (U) for all data (a, b), Regime 2 (c, d), and Regime 4 (e, f) under unstable and stable conditions, before and after removal of sub-mesoscale motions.

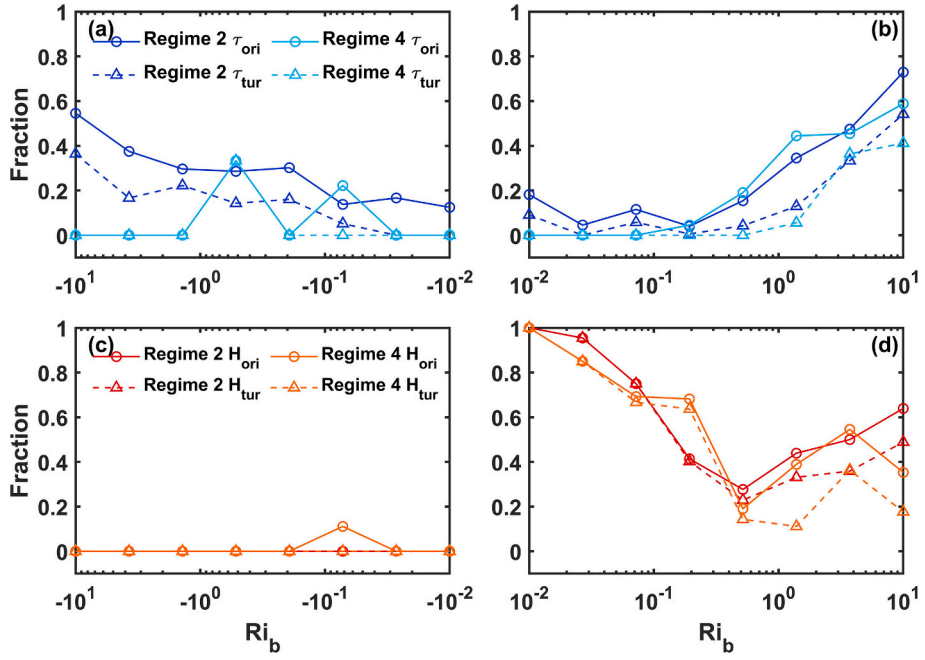

Fig. 9. Fractions of counter-gradient momentum flux (a, b) and counter-gradient sensible heat flux (c, d) as functions of bulk Richardson number for Regimes 2 and 4. Solid and dashed lines represent results from the original data and from the reconstructed turbulence, respectively.

should be noted that the regime-dependent linear correction coefficients reported here are empirical parameters derived from observations at the Tazhong site in July 2023. Their values may vary with surface characteristics. Although intermittency and sub-mesoscale motions have been documented over a wide range of surface types, the dominant types of sub-mesoscale motions may differ across surfaces, leading to different

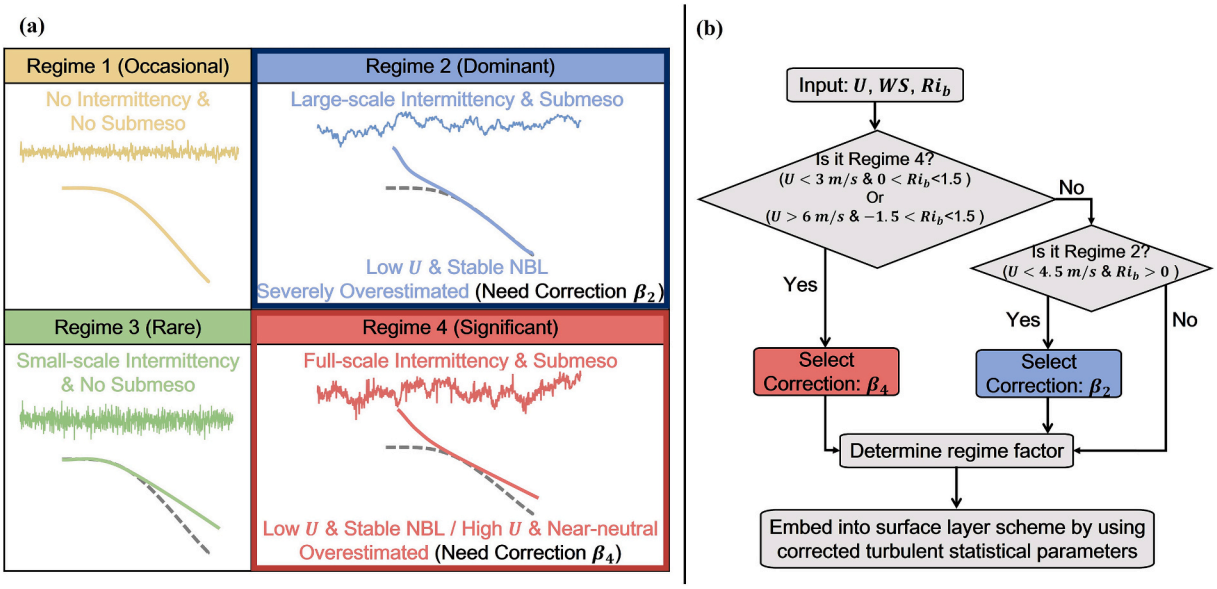

Fig. 10. Conceptual schematic integrating the four intermittency regimes and an illustrative workflow for potential model use. (a) Representative time series and spectral signatures of the four regimes, together with their typical meteorological conditions and qualitative impacts on flux and TKE estimates (Regimes 2 and 4 are most affected and require regime-dependent correction). (b) Example decision workflow using routinely available variables in models (wind speed U, wind shear WS, and bulk Richardson number Ri_b) to diagnose the most likely intermittency regime and select the corresponding correction factor (e.g., β_2 or β_4), which may be embedded into surface layer schemes by using corrected turbulent statistical parameters. Thresholds are illustrative and derived from regime-conditioned statistics in this study.

impacts on land-atmosphere exchange. In addition, the coefficient values may also vary with season and background meteorological conditions. Therefore, the values presented here are primarily intended as a reference for observational correction under summertime (July) conditions at Tazhong. For other seasons, specific synoptic situations (e.g., strongly convective periods or dust storm events), or other arid and desert sites, recalibration and validation using local observations are recommended, while keeping the same regime-identification procedure.

CRediT authorship contribution statement

Peixuan Kang: Writing – review & editing, Writing – original draft, Software, Methodology, Formal analysis, Data curation. **Yan Ren:** Writing – review & editing, Writing – original draft, Resources, Project administration, Methodology, Funding acquisition, Formal analysis, Conceptualization. **Hongsheng Zhang:** Writing – review & editing, Writing – original draft, Resources, Project administration, Funding acquisition, Conceptualization. **Wei Wei:** Writing – review & editing, Resources, Investigation, Funding acquisition. **Yue Xu:** Writing – review & editing, Resources, Investigation. **Ali Mamtimin:** Data curation. **Yu Wang:** Data curation. **Meiqi Song:** Data curation. **Jiening Liang:** Writing – review & editing, Resources, Investigation. **Lei Zhang:** Writing – review & editing, Resources, Investigation. **Jianping Huang:** Writing – review & editing, Resources, Investigation.

Declaration of competing interest

The authors declare that they have no known competing financial interests or personal relationships that could have appeared to influence the work reported in this paper.

Acknowledgments

This work was jointly funded by grant from the National Natural Science Foundation of China (42475184), Beijing Science and Technology Program Project (Z241100009124014), National Natural Science Foundation of China (42305071, 42375185) and the Longyuan Youth Talent Project.

Data availability

Data will be made available on request.

References

Banhos, J., Matheou, G., 2025. Effects of discretization of Smagorinsky–Lilly subgrid scale model on large-eddy simulation of stable boundary layers. Atmosphere 16, 310. https://doi.org/10.3390/atmos16030310.

Bou-Zeid, E., Anderson, W., Katul, G.G., Mahrt, L., 2020. The persistent challenge of surface heterogeneity in boundary-layer meteorology: a review. Boundary-Layer Meteorol. 177, 227–245. https://doi.org/10.1007/s10546-020-00551-8.

Cava, D., Mortarini, L., Anfossi, D., Giostra, U., 2019. Interaction of submeso motions in the antarctic stable boundary layer. Boundary-Layer Meteorol. 171, 151–173. https://doi.org/10.1007/s10546-019-00426-7.

Chen, Siyu, Huang, J., Kang, L., Wang, H., Ma, X., He, Y., Yuan, T., Yang, B., Huang, Z., Zhang, G., 2017a. Emission, transport, and radiative effects of mineral dust from the Taklimakan and Gobi deserts: comparison of measurements and model results. Atmos. Chem. Phys. 17, 2401–2421. https://doi.org/10.5194/acp-17-2401-2017.

Chen, SiYu, Huang, J., Li, J., Jia, R., Jiang, N., Kang, L., Ma, X., Xie, T., 2017b. Comparison of dust emissions, transport, and deposition between the Taklimakan Desert and Gobi Desert from 2007 to 2011. Sci. China Earth Sci. 60, 1338–1355. https://doi.org/10.1007/s11430-016-9051-0.

Chevillard, L., Castaing, B., Lévêque, E., Arneodo, A., 2006. Unified multifractal description of velocity increments statistics in turbulence: Intermittency and skewness. Phys. D 218, 77–82. https://doi.org/10.1016/j.physd.2006.04.011.

Conte, M., Contini, D., Held, A., 2021. Multiresolution decomposition and wavelet analysis of urban aerosol fluxes in Italy and Austria. Atmos. Res. 248, 105267. https://doi.org/10.1016/j.atmosres.2020.105267.

Durden, D.J., Nappo, C.J., Leclerc, M.Y., Duarte, H.F., Zhang, G., Parker, M.J., Kurzeja, R.J., 2013. On the impact of wave-like disturbances on turbulent fluxes and turbulence statistics in nighttime conditions: a case study. Biogeosciences 10, 8433–8443. https://doi.org/10.5194/bg-10-8433-2013.

Elshora, M., Xia, H., Su, L., Wei, T., 2024. Observation and study of consecutive dust storms in the Taklimakan desert from March 16 to 27, 2022, using reanalysis models and lidar. Atmos. Res. 305, 107431. https://doi.org/10.1016/j.atmosres.2024.107431.

Gong, S.L., Zhang, X.Y., Zhao, T.L., McKendry, I.G., Jaffe, D.A., Lu, N.M., 2003. Characterization of soil dust aerosol in China and its transport and distribution during 2001 ACE-Asia: 2. Model simulation and validation. J. Geophys. Res. 108, 2002JD002633. https://doi.org/10.1029/2002JD002633.

Hu, Z., Huang, J., Zhao, C., Bi, J., Jin, Q., Qian, Y., Leung, L.R., Feng, T., Chen, S., Ma, J., 2019. Modeling the contributions of Northern Hemisphere dust sources to dust

outflow from East Asia. Atmos. Environ. 202, 234–243. https://doi.org/10.1016/j.atmosenv.2019.01.022.
Kaimal, J.C., Wyngaard, J.C., Izumi, Y., Coté, O.R., 1972. Spectral characteristics of surface-layer turbulence. Q. J. R. Meteorol. Soc. 98, 563–589. https://doi.org/10.1002/qj.49709841707.
Klipp, C.L., Mahrt, L., 2004. Flux–gradient relationship, self-correlation and intermittency in the stable boundary layer. Q. J. R. Meteorol. Soc. 130, 2087–2103. https://doi.org/10.1256/qj.03.161.
Kolmogorov, A.N., 1941. Dissipation of energy in locally isotropic turbulence. Dokl. Akad. Nauk SSSR 32, 16–18.
Kolmogorov, A.N., 1962. A refinement of previous hypotheses concerning the local structure of turbulence in a viscous incompressible fluid at high Reynolds number. J. Fluid Mech. 13, 82–85. https://doi.org/10.1017/S0022112062000518.
Kroon, P.S., Hensen, A., Jonker, H.J.J., Ouwersloot, H.G., Vermeulen, A.T., Bosveld, F.C., 2010. Uncertainties in eddy covariance flux measurements assessed from CH4 and N2O observations. Agric. For. Meteorol. 150, 806–816. https://doi.org/10.1016/j.agrformet.2009.08.008.
Lan, C., Liu, H., Li, D., Katul, G.G., Finn, D., 2018. Distinct turbulence structures in stably stratified boundary layers with weak and strong surface shear. J. Geophys. Res. Atmos. 123, 7839–7854. https://doi.org/10.1029/2018JD028628.
Lehner, M., Rotach, M.W., 2023. The performance of a time-varying filter time under stable conditions over mountainous terrain. Boundary-Layer Meteorol. 188, 523–551. https://doi.org/10.1007/s10546-023-00824-y.
Liu, Y., He, Q., Zhang, H., Mamtimin, A., 2012. Improving the CoLM in Taklimakan Desert hinterland with accurate key parameters and an appropriate parameterization scheme. Adv. Atmos. Sci. 29, 381–390. https://doi.org/10.1007/s00376-011-1068-6.
Liu, Z., Zhang, H., Cai, X., Song, Y., 2025. Identification of non-turbulent motions for enhanced estimation of land-atmosphere transport through the anisotropy of turbulence. Earth 6, 94. https://doi.org/10.3390/earth6030094.
Mahrt, L., 1989. Intermittency of atmospheric turbulence. J. Atmos. Sci. 46, 79–95.
Mahrt, L., 1999. Stratified atmospheric boundary layers. Boundary-Layer Meteorol. 90, 375–396. https://doi.org/10.1023/A:1001765727956.
Mahrt, L., 2010. Variability and maintenance of turbulence in the very stable boundary layer. Boundary-Layer Meteorol. 135, 1–18. https://doi.org/10.1007/s10546-009-9463-6.
Mahrt, L., Bou-Zeid, E., 2020. Non-stationary boundary layers. Boundary-Layer Meteorol. 177, 189–204. https://doi.org/10.1007/s10546-020-00533-w.
Meneveau, C., Sreenivasan, K.R., 1991. The multifractal nature of turbulent energy dissipation. J. Fluid Mech. 224, 429–484. https://doi.org/10.1017/S0022112091001830.
Meng, L., Yang, X., Zhao, T., He, Q., Mamtimin, A., Wang, M., Huo, W., Yang, F., Zhou, C., Pan, H., 2020. Simulated regional transport structures and budgets of dust aerosols during a typical springtime dust storm in the Tarim Basin, Northwest China. Atmos. Res. 238, 104892. https://doi.org/10.1016/j.atmosres.2020.104892.
Obukhov, A.M., 1962. Some specific features of atmospheric turbulence. J. Geophys. Res. 67, 3011–3014. https://doi.org/10.1029/JZ067i008p03011.
Ohya, Y., Nakamura, R., Uchida, T., 2008. Intermittent bursting of turbulence in a stable boundary layer with low-level jet. Boundary-Layer Meteorol. 126, 349–363. https://doi.org/10.1007/s10546-007-9245-y.
Pfister, L., Lapo, K., Mahrt, L., Thomas, C.K., 2021. Thermal submeso motions in the nocturnal stable boundary layer. Part 2: generating mechanisms and implications. Boundary-Layer Meteorol. 180, 203–224. https://doi.org/10.1007/s10546-021-00619-z.
Ren, Y., Zhang, H., Wei, W., Wu, B., Cai, X., Song, Y., 2019. Effects of turbulence structure and urbanization on the heavy haze pollution process. Atmos. Chem. Phys. 19, 1041–1057. https://doi.org/10.5194/acp-19-1041-2019.
Ren, Y., Zhang, H., Zhang, X., Wei, W., Li, Q., Wu, B., Cai, X., Song, Y., Kang, L., Zhu, T., 2021. Turbulence barrier effect during heavy haze pollution events. Sci. Total Environ. 753, 142286. https://doi.org/10.1016/j.scitotenv.2020.142286.
Ren, Y., Zhang, H., Zhang, L., Liang, J., 2023. Quantitative description and characteristics of submeso motion and turbulence intermittency. Q. J. R. Meteorol. Soc. 149, 1726–1744. https://doi.org/10.1002/qj.4479.
Sorriso-Valvo, L., Carbone, V., Veltri, P., Politano, H., Pouquet, A., 2000. Non-Gaussian probability distribution functions in two-dimensional magnetohydrodynamic turbulence. Europhys. Lett. 51, 520–526. https://doi.org/10.1209/epl/i2000-00369-6.
Sreenivasan, K.R., Kailasnath, P., 1993. An update on the intermittency exponent in turbulence. Phys. Fluids 5, 512–514. https://doi.org/10.1063/1.858877.
Sun, J., Mahrt, L., Nappo, C., Lenschow, D.H., 2015a. Wind and temperature oscillations generated by wave–turbulence interactions in the stably stratified boundary layer. J. Atmos. Sci. 72, 1484–1503. https://doi.org/10.1175/JAS-D-14-0129.1.
Sun, J., Nappo, C.J., Mahrt, L., Belušić, D., Grisogono, B., Stauffer, D.R., Pulido, M., Staquet, C., Jiang, Q., Pouquet, A., Yagüe, C., Galperin, B., Smith, R.B., Finnigan, J. J., Mayor, S.D., Svensson, G., Grachev, A.A., Neff, W.D., 2015b. Review of wave-turbulence interactions in the stable atmospheric boundary layer. Rev. Geophys. 53, 956–993. https://doi.org/10.1002/2015RG000487.
Van De Wiel, B.J.H., Moene, A.F., Ronda, R.J., De Bruin, H.A.R., Holtslag, A.A.M., 2002. Intermittent turbulence and oscillations in the stable boundary layer over land. Part II: a System dynamics approach. J. Atmos. Sci. 59, 2567–2581. https://doi.org/10.1175/1520-0469(2002)059<2567:ITAOIT>2.0.CO;2.
Vercauteren, N., Boyko, V., Kaiser, A., Belušić, D., 2019. Statistical investigation of flow structures in different regimes of the stable boundary layer. Boundary-Layer Meteorol. 173, 143–164. https://doi.org/10.1007/s10546-019-00464-1.
Vickers, D., Mahrt, L., 1997. Quality control and flux sampling problems for tower and aircraft data. J. Atmos. Ocean. Technol. 14, 512–526. https://doi.org/10.1175/1520-0426(1997)014<0512:QCAFSP>2.0.CO;2.
Wang, M., Wei, W., He, Q., Yang, Y., Fan, L., Zhang, J., 2016. Summer atmospheric boundary layer structure in the hinterland of Taklimakan Desert, China. J. Arid. Land 8, 846–860. https://doi.org/10.1007/s40333-016-0054-3.
Wang, M., Xu, X., Xu, H., Lenschow, D.H., Zhou, M., Zhang, J., Wang, Y., 2019. Features of the deep atmospheric boundary layer over the taklimakan desert in the summertime and its influence on regional circulation. J. Geophys. Res. Atmos. 124, 12755–12772. https://doi.org/10.1029/2019JD030714.
Wei, W., Wang, M., Zhang, H., He, Q., Ali, M., Wang, Y., 2019. Diurnal characteristics of turbulent intermittency in the Taklimakan Desert. Meteorog. Atmos. Phys. 131, 287–297. https://doi.org/10.1007/s00703-017-0572-3.
Wei, Z., Zhang, H., Wei, W., Zhang, X., Cai, X., Song, Y., Zhu, T., 2022. Mechanism of the effect of vertically propagating internal gravity waves on turbulence barrier and pollutant diffusion during heavy haze episodes. Sci. Total Environ. 845, 157349. https://doi.org/10.1016/j.scitotenv.2022.157349.
Xiong, Z., Xu, X., Yang, Y., Luo, T., 2023. Diurnal vertical distribution and transport of dust aerosol over and around Tibetan Plateau from lidar on International Space Station. Atmos. Res. 294, 106939. https://doi.org/10.1016/j.atmosres.2023.106939.
Xu, H., Wang, M., Wang, Y., Cai, W., 2018. Performance of WRF large eddy simulations in modeling the convective boundary layer over the Taklimakan Desert, China. J. Meteorol. Res. 32, 1011–1025. https://doi.org/10.1007/s13351-018-8001-1.
Zhang, X.Y., Gong, S.L., Zhao, T.L., Arimoto, R., Wang, Y.Q., Zhou, Z.J., 2003. Sources of Asian dust and role of climate change versus desertification in Asian dust emission. Geophys. Res. Lett. 30, 2003GL018206. https://doi.org/10.1029/2003GL018206.
Zhang, B., Tsunekawa, A., Tsubo, M., 2008. Contributions of sandy lands and stony deserts to long-distance dust emission in China and Mongolia during 2000–2006. Glob. Planet. Chang. 60, 487–504. https://doi.org/10.1016/j.gloplacha.2007.06.001.